Adsorption of Ciprofloxacin onto Lotus Stem-Derived Biochar: Effects of Solution pH, Temperature, And Coexisting Cations

Vo Nguyen Lam Uyen[1,2], Vo Duc Hieu[1,2], Dang Thanh Minh Khoi[1,2], Pham Duy Tan[1,2], Ly Quoc Nguyen Khang[1,2], Nguyen Le The Quang[1,2], Nguyen Trong Bang[1,2], Phan Trung Hieu[1,2], Bao-Trong Dang[1,2,*]

[1]*Faculty of Chemical Engineering, Ho Chi Minh City University of Technology (HCMUT), 268 Ly Thuong Kiet Street, Dien Hong Ward, Ho Chi Minh City, Vietnam.*

[2]*Vietnam National University Ho Chi Minh City, Linh Trung Ward, Ho Chi Minh City, Vietnam.*

**Corresponding author. E-mail: dbaotrong@hcmut.edu.vn (B.-T. Dang). Tel: +84 338199939*

List ORCID iDs:

- Vo Nguyen Lam Uyen — https://orcid.org/0009-0002-4364-8870
- Vo Duc Hieu — https://orcid.org/0009-0008-1046-223X
- Dang Thanh Minh Khoi — https://orcid.org/0009-0003-1222-5119
- Pham Duy Tan — https://orcid.org/0009-0001-9325-5832
- Ly Quoc Nguyen Khang — https://orcid.org/0009-0007-8009-5546
- Nguyen Le The Quang — https://orcid.org/0009-0001-9060-1242
- Nguyen Trong Bang — https://orcid.org/0009-0006-0309-7006
- Phan Trung Hieu — https://orcid.org/0009-0004-7559-9473
- Bao-Trong Dang — https://orcid.org/0000-0002-4538-0591

Abstract

The discharge of ciprofloxacin (CFX) into aquatic environments poses a threat to ecosystem health. In this study, biochar derived from lotus stem (*Nelumbo nucifera*) was evaluated as a low-cost adsorbent for CFX removal from aqueous solution. The biochar was characterized by SEM/EDX, N_2 adsorption-desorption isotherms, FTIR, and point of zero charge (pH_{pzc}). Batch sorption experiments were conducted to examine the effects of solution pH (3, 7, and 10), temperature (20, 26, and 32 °C), and coexisting cations. The kinetics of sorption could be explained using a two-stage intraparticle diffusion model, and the equilibrium isotherms were fitted to the Langmuir model. The maximum adsorption capacity (Q_{max}) was 22.96 mmol kg^{-1} at pH 7 and 26 °C. Solution pH influenced the sorption capacity, yet substantial sorption was maintained across the entire pH range studied. Thermodynamic analysis revealed an endothermic, entropy-driven and spontaneous process at all temperatures. Divalent Ca^{2+} suppressed Q_{max} by 49.0% through competition with CFX for adsorption sites. The sorption process under pH 7 was facilitated by electrostatic attraction, hydrogen bonding, and π–π stacking interactions. Overall, unmodified lotus stem biochar proved to be a promising and cost-effective adsorbent for CFX removal from water.

Keywords: c*iprofloxacin; biochar; lotus stem; adsorption; coexisting cations; thermodynamic analysis.*

1. Introduction

Antibiotics have become ubiquitous aquatic pollutants due to their increasing use in agriculture and medicine. Because a large portion is excreted unmetabolized, antibiotics enter water bodies through hospital, pharmaceutical, and municipal wastewater streams [1,2]. Conventional biological treatments fail to mineralize the stable structures of antibiotics, leading to their persistent presence in the environment [3,4]. Consequently, sub-inhibitory concentrations exert sustained selective pressure on aquatic microbiomes, accelerating antimicrobial resistance (AMR), a critical global health threat [5–7]. As a result, effective post-treatment technologies are urgently needed.

Ciprofloxacin (CFX; $C_{17}H_{18}FN_3O_3$; M = 331.34 g mol^{-1}), a widely prescribed broad-spectrum fluoroquinolone, is frequently detected in environmental waters at nanogram-to-microgram per litre levels. CFX is resistant to biodegradation because it targets bacterial DNA gyrase and topoisomerase IV. The environmental fate of CFX is governed by its amphoteric character ($pK_{a1} \approx 6.1$; $pK_{a2} \approx 8.7$), where pH-dependent speciation yields a large fraction of CFX^+ at pH < 6.1, $CFX^{\pm}$ at pH 6.1–8.7, and CFX^- at pH > 8.7 [8]. This speciation has a significant impact on CFX interactions with adsorbent surfaces, which is important for the design of removal systems.

Despite achieving high CFX removal rates, advanced oxidation and membrane technologies are limited by prohibitively high capital costs and operational complexity. This issue is especially relevant in resource-constrained settings in developing countries, where antibiotics are widely used and cause pollution. Therefore, sorption using inexpensive solid sorbents remains the most feasible option from both economic and efficiency standpoints. Among various solid sorbents, biochar has emerged as a potential material for sequestering carbon and antibiotics. However, the feedstock and pyrolysis conditions significantly influence the sorption characteristics of biochar. At moderate pyrolysis temperatures (e.g., 400 °C), biochar retains a significant amount of oxygen-containing functional groups that act as active

sites for hydrogen bonding and electrostatic interactions with polar adsorbates. Additionally, it develops incipient aromatic domains capable of π–π electron donor–acceptor interactions [9–11].

Among various biomasses, the lotus (*Nelumbo nucifera*) generates substantial biomass in Asia, serving as an important precursor for biochar production [12]. Lotus-derived biochar exhibits exceptional versatility in remediating diverse environmental contaminants, effectively eliminating heavy metals [13], adsorbing organic dyes like methyl orange [14], capturing carbamate pesticides [15], and catalyzing heavy oil degradation [16]. However, there have been no reports of using unmodified lotus stem biochar to remove CFX, although it has been demonstrated to be effective on a variety of pollutants. As a result, it remained unclear how solution chemistry factors such as pH and background cations influenced CFX sorption onto this material. For example, pH-modulated antibiotic speciation and biochar surface charge can alter removal pathways and influence binding affinity [10,17].

CFX adsorption has been investigated on pinewood biochar [11], chitosan/biochar composites [18], and surface-modified biochars [3,19,20] , with widely varying capacities. According to reports, adsorption is very sensitive to CFX speciation [4], and divalent cations exhibit competitive electrostatic interactions and chelation with the carboxylate and amine groups of CFX [21,22]. There is currently no research that examines these factors for unmodified lotus stem biochar, however.

Therefore, this study aimed to investigate the adsorption behavior of CFX onto biochar (BC) derived from *Nelumbo nucifera* stem petioles produced by slow pyrolysis at 400 °C. Sorption kinetics and equilibrium isotherms were evaluated at three pH levels (3, 7, 10), three temperatures (20, 26, 32 °C), and in the presence of coexisting mono- and divalent cations (Na^+ and Ca^{2+}). Thermodynamic parameters were calculated using the Van't Hoff equation. To the best of our knowledge, this study is the first systematic investigation of CFX adsorption by unmodified lotus stem biochar, integrating solution speciation and competitive ionic matrix

effects within a unified mechanistic framework, and contributing to the valorization of agricultural residues as cost-effective antibiotic adsorbents.

2. Materials and methods

2.1. Reagents and materials

Ciprofloxacin (CFX; purity ≥ 98%, Acros Organics) was used as the target adsorbate without further purification. Stock solutions of 1000 mg L^{-1} were prepared by dissolving CFX in doubly distilled water and stored at 4 °C in the dark. Working solutions were prepared daily by serial dilution. Sodium hydroxide (NaOH, AR grade, Xilong Chemical) and hydrochloric acid (HCl, AR grade, Xilong Chemical) were used to adjust the pH. Sodium chloride (NaCl, AR, Xilong Chemical), calcium chloride ($CaCl_2$, AR, Xilong Chemical) were used in background ionic strength experiments. All solutions were prepared with doubly distilled water.

2.2. Preparation of biochar

Lotus stems (*Nelumbo nucifera*) were collected from local ponds in the Mekong Delta region of Vietnam. The raw material was washed thoroughly with tap water followed by doubly distilled water to remove surface impurities, cut into small pieces (~3-5 cm), and oven-dried at 105 °C for 24 h. The dried biomass was placed in a muffle furnace (without N_2 gas protection) and pyrolyzed at 400 °C with a heating rate of 10 °C min^{-1} and held at the target temperature for 2 h. Pyrolysis in a muffle furnace serves as a simple and cost-effective method that produces biochars with sorption performance comparable to those obtained in a tube furnace and traditional kilns [23,24]. The resulting biochar was allowed to cool naturally to room temperature, then ground and sieved. The product was washed until the solution reached a pH of 7, then stored in a desiccator before use.

2.3. Characterization of biochar

The specific surface area (SSA), total pore volume, and average pore diameter of BC were determined by N_2 adsorption–desorption at 77 K using a surface area analyser (Quantachrome

NOVA 1000e, USA). Surface morphology and elemental composition were examined by field-emission scanning electron microscopy coupled with energy-dispersive X-ray spectroscopy (FESEM/EDX; HITACHI S-4800, Japan; HORIBA EDX H-7593, UK). Surface functional groups were identified by Fourier-transform infrared spectroscopy (FTIR; PerkinElmer NIR/MIR Frontier) in the range 400–4000 cm^{-1} at 1 cm^{-1} resolution and 50 scans per spectrum. FTIR spectra were collected for both pristine biochar and for samples recovered after CFX adsorption.

The point of zero charge (pH_{pzc}) was determined by the pH drift method [25]. A series of 25 mL aliquots of 0.1 M KCl solution was adjusted to initial pH values (pH_0) of 2–11 using 0.1 M NaOH and 0.1 M HCl. To each, 0.1 g of biochar was added, and suspensions were agitated at 120 rpm for 24 h at room temperature. Final pH (pH^f) was recorded after filtration, and ΔpH (= $pH^f - pH_0$) was plotted against pH_0. The pH_{pzc} was identified as the intercept of the ΔpH versus pH_0 curve with the x-axis.

2.4. Adsorption experiments

2.4.1. Sorption kinetics

The kinetic adsorption was studied by preparing a CFX solution with an initial concentration of 16 mg/L in a 250 mL beaker. The solution pH was adjusted to 7 using 0.1 M NaOH and 0.1 M HCl solutions. Subsequently, 0.5 g of biochar was added to the beaker, and the mixture was stirred using a magnetic stirrer at 120 rpm at 26 °C room temperature. The biochar dosage was fixed at 2.0 g/L [26]. Aliquots were withdrawn at predetermined time intervals from 0 to 1440 min, immediately filtered through 0.45 µm syringe filters, and analyzed by UV–Vis spectrophotometry (Jasco V-730, Japan). For aqueous solutions at pH 7, absorbance was measured at 271 nm [27] and quantified using the calibration equation (R^2=0.9999). Kinetic data were fitted to the nonlinear pseudo-first order (PFO), pseudo-second order (PSO) model and two stage-intraparticle diffusion model (two stage-IPD) [28] (Eqs. 1–4):

$$\text{PFO: } q_t = q_{max}\,(1 - e^{-k1t}) \qquad (1)$$

$$\text{PSO: } q_t = (q_e^2\, k_2\, t)\,/\,(1 + q_e\, k_2\, t) \qquad (2)$$

$$\text{two-stage-IPD: } q_t = k_1^{stage1}\, t^{1/2} \quad 0 \le t \le t_1 \qquad (3)$$

$$q_t - q_{t=t1} = k_2^{stage2}\,(t - t_1)^{1/2} \quad t_1 < t \le t_2 \qquad (4)$$

where q_{max} and q_e (mmol kg $^{-1}$): the sorption capacities of the PFO and PSO models.

q_t (mmol kg $^{-1}$): the sorption capacity at time t;

k_1 (min^{-1}) and k_2 (kg mmol^{-1} min^{-1}): the rate constants for PFO and PSO, respectively.

k_1^{stage1} and k_2^{stage2} (mmol kg^{-1} min$^{-1/2}$): the rate constants of the two stage-IPD;

t_1: time for quasi-equilibrium of solute concentrations is reached.

Several criteria have been established to select the appropriate model, including the second-order Akaike Information Criterion (*AICc*), the Shapiro–Wilk test, the *p-value*, adjusted R-squared (adj-R^2) [4]

2.4.2. Adsorption isotherms

Equilibrium isotherm experiments were performed in a centrifuge tube containing 10 mL of CFX solution at initial concentrations of 12–80 mg L^{-1}. 0.02 g of biochar was added, and the tubes were shaken at 26°C. Samples were agitated at 120 rpm in a temperature-controlled shaker at the target temperature until adsorption equilibrium was confirmed (≥ 8 h, based on kinetic results). After equilibration, suspensions were filtered through 0.45 μm syringe filters and analyzed by UV–Vis spectrophotometry. Equilibrium data were described by the nonlinear Langmuir isotherm (Eq. 5):

$$Q_e = (Q_{max}\, K_L\, C_e) / (1 + K_L\, C_e) \qquad (5)$$

where Q_{max} (mmol kg^{-1}) is the maximum monolayer adsorption capacity, K_L (L mmol^{-1}) is the Langmuir affinity constant, and C_e (mmol L^{-1}) is the equilibrium liquid-phase concentration.

The Freundlich model was also applied. Parameter estimation was performed by nonlinear least-squares regression.

2.4.3. Effect of solution pH

To evaluate the effect of solution pH on adsorption capacity, isotherm experiments were conducted at pH 3, 7, and 10, following the general procedure described above. pH was adjusted using 0.1 M NaOH and 0.1 M HCl and verified with a calibrated pH meter (Hanna Instruments HI 2210, USA). Experiments were conducted at 26 °C in the temperature-controlled shaker. For aqueous solutions at pH3 and 10, absorbance was measured at 277 nm and 272 nm [27]

2.4.4. Effect of background cations

The influence of coexisting cations on CFX adsorption was investigated by adding 1 mL of concentrated salt solutions (0.1 M) of NaCl and $CaCl_2$, to each adsorption system, yielding final cation concentrations of 10 mM for monovalent (Na^+) and divalent (Ca^{2+}) species. Experiments were conducted at pH 7 and 26 °C. For solutions containing cations ions, absorbance was measured at 272 nm. A control system without added cations was run in parallel under identical conditions.

2.5. Thermodynamic calculations

Thermodynamic parameters were derived from thermodynamic equilibrium constants obtained at three temperatures (20, 26, and 32 °C; pH 7) using the Van't Hoff equation (Eq. 6):

$$\ln K_c = -\Delta H^\circ / (RT) + \Delta S^\circ / R \qquad (6)$$

where K_c (dimensionless) is the thermodynamic equilibrium constant obtained by converting the Langmuir K_L (L $mmol^{-1}$) to a dimensionless form, R is the universal gas constant (8.314 J mol^{-1} K^{-1}), and T is the absolute temperature (K).

The estimated K_L (L mmol^{-1}) was transformed to approximately K_c (*Eq. 7)* using the activity coefficient (γ_e) of the adsorbate and the molar concentration of the standard reference solution (C_s), which is equal to 1 mol L^{-1}.

$$K_c = (1000\ K_L\ C_s)/\gamma_e \quad (7)$$

According to the Debye-Hückel law, the activity coefficient $\gamma_e \approx 1$ for neutral or weak charged adsorbates and $K_c \approx 1000\ K_L$.

The standard Gibbs free energy change (ΔG°, kJ mol^{-1}), standard enthalpy change (ΔH°, kJ mol^{-1}) and standard entropy change (ΔS°, J mol^{-1} K^{-1}) was calculated at each temperature as (Eq. 8):

$$\Delta G° = \Delta H° - T\ \Delta S° \quad (8)$$

3. Results and discussion

3.1. Characterization of BC

As shown in Fig. 1a, the SEM image revealed a mixed porous and compact surface morphology for biochar produced at a pyrolysis temperature of 400 °C. EDX analysis confirmed that carbon was the dominant element (Fig. 1b), accounting for 87.65 ± 0.11 wt%, while oxygen accounted for 11.30 ± 0.11 wt% (Table 1).

The low O/C ratio (0.13) suggests significant removal of oxygen-containing functionalities during pyrolysis. Small amounts of sulfur (0.32 ± 0.02 wt%) and calcium (0.73 ± 0.05 wt%) were also detected. The O/C ratio of BC (0.13) is markedly lower than that of other biochars pyrolyzed at comparable moderate temperatures (300–500 °C with N_2 gas), including coconut shell biochar CN400 (O/C = 0.17) [28], corn cob biochar CC400 (O/C ≈ 0.27) [29], cassava peel biochar CP500 (O/C = 0.18) [4].

Table 1. Selected physicochemical properties of the biochar

Parameters	**Units**	
Pyrolysis temperatures	°C	400
Residence time	h	2
Heating rate	°C min^{-1}	10
N_2 gas protection	-	None
Biochar yield	%	29.92 ± 0.68
EDX and Surface Properties		
C using EDX	wt%	87.65 ± 0.11
O using EDX	wt%	11.30 ± 0.11
O/C ratio (mass ratio)	–	0.13
S using EDX	wt%	0.32 ± 0.02
Ca using EDX	wt%	0.73 ± 0.05
SSA using Langmuir	m^2 g^{-1}	53.175

This suggests that lotus stem biomass undergoes more extensive thermal decomposition of oxygenated functionalities than conventional lignocellulosic and marine feedstocks, likely reflecting the hemicellulose-rich of aquatic macrophyte stems. The FTIR spectra further confirmed that pyrolysis significantly changed the surface chemistry (Fig. 1c). In the raw biomass, a broad and intense band centered at 3447 cm^{-1} was observed, which weakened and shifted to 3416 cm^{-1} in BC, indicating a reduction in hydroxyl-related structures during carbonization. The band at 1633 cm^{-1} in the raw lotus shifted to 1612 cm^{-1} after pyrolysis. This suggests structural reorganization of the carbon matrix and increased contributions from unsaturated or aromatic C=C vibrations. A more noticeable change was seen for the C–O-related band, which moved from 1108 cm^{-1} in the raw material to 1163 cm^{-1}. This reflects modifications to oxygen-containing functionalities after thermal treatment.

As shown in Fig. 1d, the N_2 adsorption–desorption data were further analyzed using the Langmuir equation to determine the surface area. The linear plot showed excellent linearity with $y = 65.50\ x + 13.69$ ($R^2 = 0.997$). The Langmuir surface area was estimated at 53.175 m^2 g^{-1}, indicating that the biochar possesses a measurable accessible surface. The Langmuir-derived SSA is higher than that of other biochars pyrolyzed at 400 °C, including coconut shell biochar (4.06 m^2 g^{-1}) [28], corn cob (4.8 m^2 g^{-1}) [29], and Sargassum polycystum (11.7 m^2 g^{-1})

[30], and even exceeds that of cassava peel (29.45 m^2 g^{-1}) pyrolyzed at a higher temperature 500 °C [4]. The pH_{pzc} of the biochar was determined to be approximately 6.0 by the pH-drift method (Table 1). Overall, lotus biochar produced at moderate-temperature pyrolysis exhibited a carbon-rich composition with a low O/C ratio. The Langmuir surface area indicated a moderately developed pore structure. FTIR analysis confirmed that pyrolysis reduced hydroxyl-related groups while promoting aromatic C=C and C–O groups. The coexistence of residual oxygen-containing functional groups and accessible porosity suggests that this biochar may support both surface-driven interactions and pore-filling mechanisms.

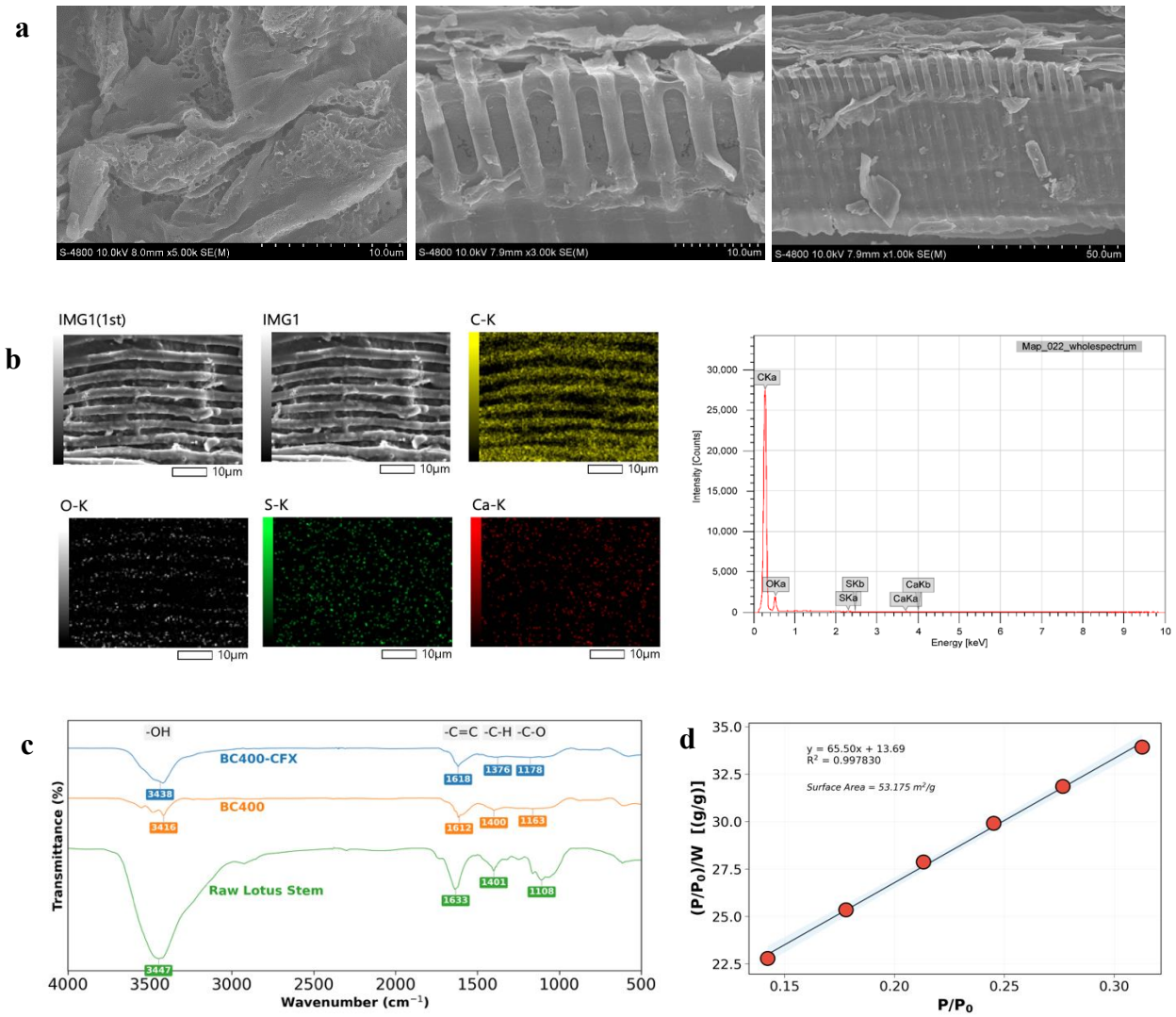

Fig. 1. SEM image (a), EDX spectrum/mapping (b), FTIR spectra (c), and Langmuir plot derived from N_2 adsorption–desorption data (d).

3.2. Sorption kinetics at pH 7 and 26 °C

The nonlinear kinetic fitting results for CFX sorption are presented in Table 2. The PSO model provided a better fit than the PFO model, with the higher adjusted coefficient of determination (Adj-R^2: 0.904 vs. 0.738). However, the two-stage IPD model provided the best overall fit, with the highest adjusted R^2 (0.984) and the lowest AICc (−14.598). This suggests that CFX uptake did not proceed through a single kinetic step. The fitted IPD parameters showed a much faster first stage (k_1 = 2.775 ± 0.112 mmol kg^{-1} $min^{-1/2}$) followed by a slower second stage (k_2 = 0.117 ± 0.010 mmol kg^{-1} $min^{-1/2}$), with a transition time t_1 of 11 min. This pattern indicates a rapid initial uptake, likely associated with pore diffusion, followed by a slower diffusion-controlled stage.

Table 2. PFO and PSO and Two-Stage IPD kinetic parameters (C_0 = 16 mg L^{-1}, pH 7, 26 °C).

Model	Parameter	Estimate	Std.Error	p-value	Adj-R^2	AICc	Shapiro.p
PFO	q_e	11.090	0.499	0.000	0.738	45.112	0.801
	k_1	0.158	0.038	0.003			
PSO	q_e	11.770	0.350	0.000	0.904	34.033	0.693
	k_2	0.0187	0.004	0.001			
Two-Stage IPD	k_1 (Stage 1)	2.775	0.112	0.002	0.984	-14.598	0.323
	k_2 (Stage 2)	0.117	0.010	0.000			
	t_1	11					

3.3. Effect of pH on the adsorption isotherm

The adsorption isotherms of CFX were evaluated at pH 3, 7, and 10 to examine the effect of solution pH (Fig. 2a). The equilibrium data were fitted using both the Langmuir and Freundlich models, and the fitted parameters are summarized in Table 3. Both models described the data well, with adjusted R^2 values ranging from 0.874 to 0.986. The Freundlich model gave a slightly better fit at pH 3 and 10, whereas the Langmuir model performed better at pH 7 (Adj-R^2 = 0.974). The Langmuir maximum adsorption capacity, Q_{max}, varied with pH and followed

the order pH 7 (22.96 mmol kg^{-1}) ≈ pH 10 (22.88 mmol kg^{-1}) > pH 3 (20.70 mmol kg^{-1}). BC maintained high CFX uptake across acidic, neutral, and alkaline conditions. This potential improvement in pollutant removal is noteworthy. At a pH of 7, lotus stem biochar exhibited a Q_{max} that exceeded the capacities reported for conventional biochar derived from agricultural waste such as groundnut shell (6.9 mmol kg^{-1}) [31], cassava peel (10.5 mmol kg^{-1}) [4], and rice straw (11.2 mmol kg^{-1}) [32].

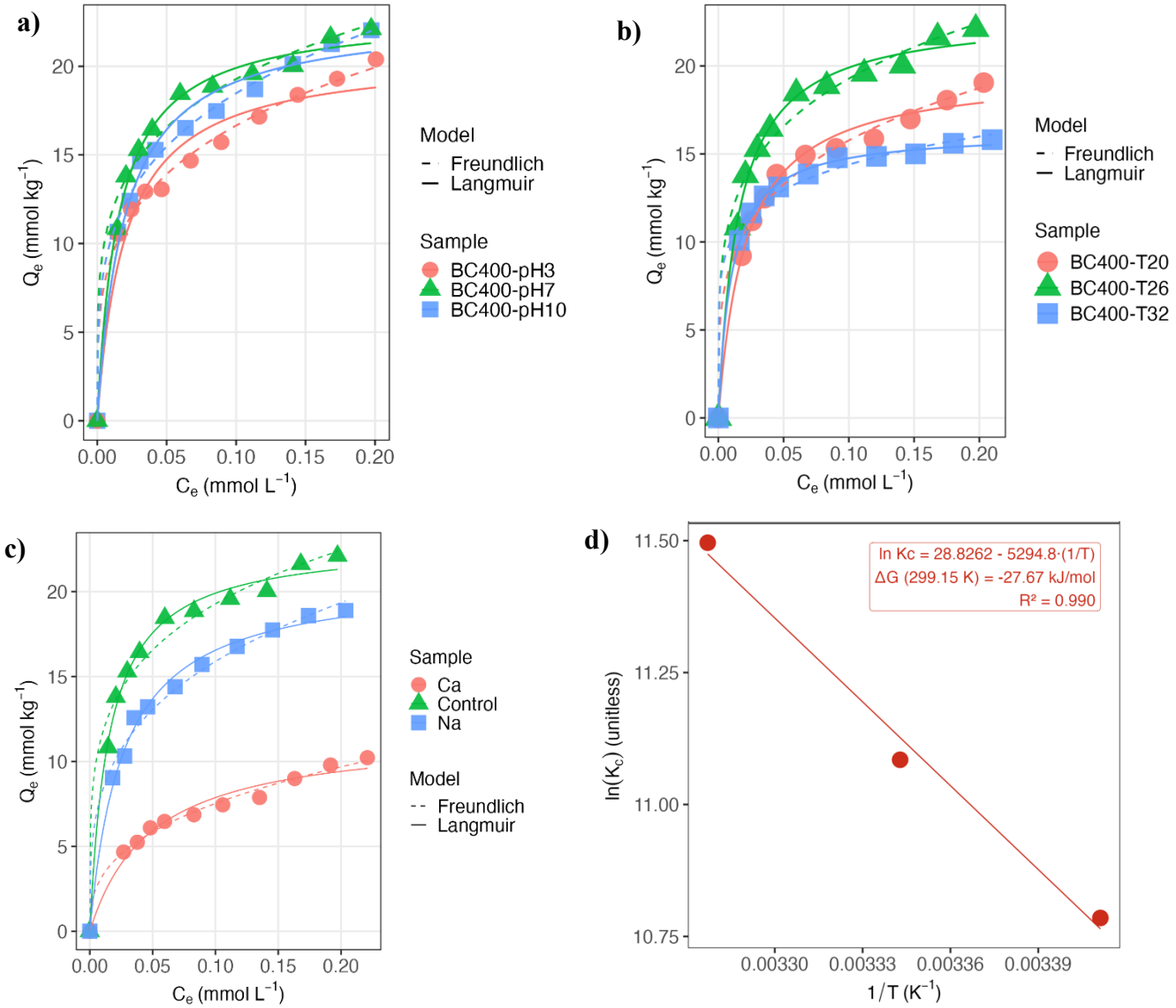

Fig. 2. Langmuir and Freundlich isotherm models under varying solution pH (a); temperature (b); ionic composition (c), and Van't Hoff Plot (d).

From Table 3, the K_L was also highest at pH 7 (65.16 L $mmol^{-1}$), suggesting stronger overall affinity at near-neutral pH. By contrast, the lower uptake at pH 3 can be attributed to less

favorable surface–solute interactions under acidic conditions. This can be interpreted in relation to the pH-dependent speciation of CFX and the surface charge of BC. At pH 3**,** CFX is expected to occur mainly in its cationic form (CFX^+, 99%), while the BC surface is also positively charged. Under these conditions, electrostatic attraction is reduced. However, the adsorption capacity remained substantial, suggesting that non-electrostatic interactions still contributed significantly. At pH 7, CFX is expected to be predominantly zwitterionic **(**$CFX^{\pm}$, 87.2%**)**. This condition may provide a more favorable balance between electrostatic effects and other interactions. FTIR analysis of BC after CFX sorption at pH 7 revealed shifts in the –OH stretching band (3416 → 3438 cm^{-1}), aromatic C=C vibration (1612 → 1618 cm^{-1}), and C–O stretching (1163 → 1178 cm^{-1}), accompanied by a reduction in overall peak intensity. This attributed to the involvement of hydrogen bonding, π–π interactions, and oxygen-containing functional groups in CFX sorption.

Table 3. Isotherm parameters of Langmuir and Freundlich isotherm under varying solution pH, temperature, and ionic composition.

Sample	Model	Parameter	Estimate	SD	p-value	Adj-R^2	AICc	Shapiro-p
pH 3	Langmuir	Q_{max}	20.698	0.951	0.000	0.874	39.495	0.376
		K_L	49.578	9.693	0.001			
	Freundlich	K_f	30.279	0.813	0.000	0.986	17.393	0.277
		n	3.852	0.161	0.000			
pH 7	Langmuir	Q_{max}	22.962	0.418	0.000	0.974	25.197	0.375
		K_L	65.168	5.495	0.000			
	Freundlich	K_f	31.934	1.651	0.000	0.938	33.885	0.688
		n	4.563	0.415	0.000			
pH 10	Langmuir	Q_{max}	22.876	0.693	0.000	0.946	33.311	0.578
		K_L	50.966	6.475	0.000			
	Freundlich	K_f	33.334	1.020	0.000	0.983	22.073	0.663
		n	3.902	0.185	0.000			
T20	Langmuir	Q_{max}	19.749	0.517	0.000	0.958	27.026	0.900
		K_L	48.290	5.332	0.000			
	Freundlich	K_f	27.983	1.269	0.000	0.958	26.824	0.977
		n	4.015	0.295	0.000			

T26	Langmuir	Q_{max}	22.962	0.418	0.000	0.974	25.197	0.375
		K_L	65.168	5.495	0.000			
	Freundlich	K_f	31.934	1.651	0.000	0.938	33.885	0.688
		n	4.563	0.415	0.000			
T32	Langmuir	Q_{max}	16.260	0.141	0.000	0.986	6.145	0.573
		K_L	98.331	5.357	0.000			
	Freundlich	K_f	20.431	0.668	0.000	0.945	19.492	0.836
		n	6.573	0.547	0.000			
Ca	Langmuir	Q_{max}	11.704	0.651	0.000	0.926	22.595	0.381
		K_L	20.526	3.459	0.000			
	Freundlich	K_f	17.374	0.743	0.000	0.978	10.440	0.519
		n	2.751	0.146	0.000			
Control	Langmuir	Q_{max}	22.962	0.418	0.000	0.974	25.197	0.375
		K_L	65.168	5.495	0.000			
	Freundlich	K_f	31.934	1.651	0.000	0.938	33.885	0.688
		n	4.563	0.415	0.000			
Na	Langmuir	Q_{max}	20.911	0.441	0.000	0.980	21.476	0.430
		K_L	37.896	3.002	0.000			
	Freundlich	K_f	30.555	1.208	0.000	0.975	23.822	0.365
		n	3.520	0.201	0.000			

[a] *The units are follows: Q_{max} in mmol kg^{-1}, K_L in L mmol^{-1}, K_F in mmol^{1-n} L^n/kg. K_F is the Freundlich affinity coefficient and n are the heterogeneity factor (dimensionless).*

3.4. Effect of temperature on adsorption

Adsorption isotherms were conducted at 20, 26, and 32 °C to investigate the thermal dependence of CFX uptake on BC (Fig 2b, Table 3). At constant pH 7, Q_{max} showed a non-monotonic response to temperature. Q_{max} increased from 19.75 mmol kg^{-1} at 20 °C to 22.96 mmol kg^{-1} at 26 °C, then decreased to 16.26 mmol kg^{-1} at 32 °C. The initial increase from 20 to 26 °C is consistent with the endothermic character of adsorption. The elevated temperature provides additional thermal energy to overcome activation barriers for surface site occupancy and intraparticle diffusion. The subsequent decline at 32 °C is attributed to the increasing desorption rate at higher thermal energy. The inverse trend between K_L and Q_{max} at 32 °C suggests that elevated temperature strengthened individual binding interactions while

simultaneously reducing the number of weak sorption sites. Across the tropical temperature range (20–32 °C), Q_{max} exhibited moderate variation (17.1%), yet remained consistently above 16 mmol kg^{-1} under all conditions tested.

3.5. Sorption thermodynamics

Thermodynamic parameters derived from Van't Hoff analysis at pH 7 are presented in Table 4 and Fig. 2d. Specifically, ΔG° ranged from −26.24 kJ mol^{-1} (20 °C) to −29.11 kJ mol^{-1} (32 °C). The ΔG° was negative at all temperatures examined, confirming that CFX adsorption onto BC is spontaneous. The increase in |ΔG°| with temperature confirms that a higher temperature enhances the thermodynamic driving force for sorption. However, the maximum adsorption capacity increased from 20 to 26 °C and then decreased at 32 °C. This can be explained by the fact that the ΔG° value is governed by K_c [28–30], which varies with temperature, and its trend may not coincide with that of Q_{max}. Q_{max} is influenced by specific interactions inherent to the heterogeneous surface [28–30]. The increased thermal energy, coupled with the entropy gain, facilitates the desorption of molecules, thereby reducing the Q_{max}. Similar phenomena have been observed for other materials, such as hematite, iron-loaded sludge biochar, and pigeon pea husk, used to adsorb antibiotics or other substances [33–36] The standard enthalpy changes ΔH° was positive (+44.02 kJ mol^{-1}), unambiguously establishing the endothermic nature of CFX adsorption onto BC. Endothermic adsorption arises when the thermal energy required to desorb water molecules from both the adsorbent surface (hydration sphere disruption) and the CFX hydration shell exceeds the enthalpy released upon CFX–surface bond formation. The ΔH° value of 44.02 kJ mol^{-1} exceeds the typical physisorption threshold (< 20 kJ mol^{-1}), indicating the involvement of stronger, chemically specific interactions in addition to physical forces. This is consistent with a mixed physico-chemical adsorption mechanism involving simultaneous electrostatic, π–π stacking, and hydrogen-bonding interactions [9,19]. The ΔS° was large and positive (+239.66 J mol^{-1} K^{-1}). Large positive ΔS° values are attributed to structural rearrangement at the solid–liquid interface. The large positive TΔS° term overcomes

the energetic cost of $\Delta H° > 0$, rendering $\Delta G° = \Delta H° - T\Delta S°$ negative and adsorption spontaneous.

Table 4. Thermodynamic parameters for CFX adsorption onto BC

Temperature (K)	K_L (L.mmol^{-1})	ΔH^0 (kJ.mol^{-1})	ΔS^0 (J/mol.K)	ΔG^0 (kJ.mol^{-1})	Adj-R^2
293.15	48.29			-26.236	
299.15	65.168	44.021	239.661	-27.674	0.979
305.15	98.331			-29.112	

3.6. Effect of coexisting cations

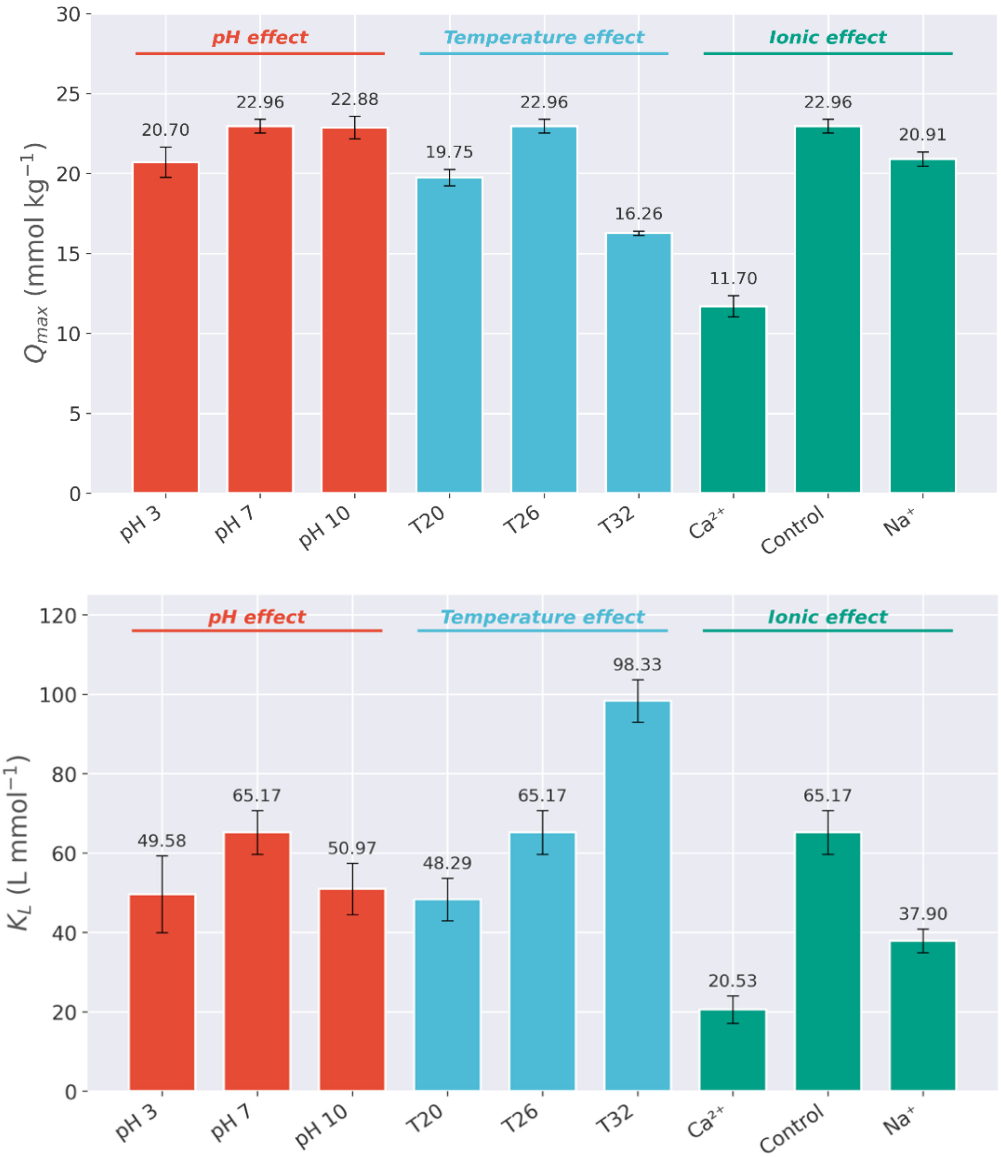

Fig. 3. Comparison of Langmuir parameters in the presence of different cations.

The influence of background mono- and divalent cations on the CFX adsorption at pH 7 and 26 °C is summarized in Fig 2c and Table 3. In the absence of added cations (control), Q_{max} was 22.96 mmol kg^{-1}. Addition of monovalent Na^+ caused only modest reductions to 20.91 mmol kg^{-1}, corresponding to capacity decreases of ~ 9 %. The K_L reduced by 42%. The suppression by Na^+ suggests that there is competitive adsorption at the surface sites of biochar. However, the minor suppression observed is also attributed to ionic strength effects, as increased ionic strength compresses the electrical double layer around the biochar surface, partially screening the electrostatic attraction between the piperazinyl nitrogen of $CFX^{\pm}$ and negatively charged surface sites [21,22]. Our observed 9% capacity loss under higher Na^+ concentrations is consistent with previous studies [37]. Specifically, higher electrolyte levels weaken the attraction between the negative surface of the adsorbent and the antibiotic's amino groups.

In sharp contrast, divalent cations caused severe and differentiated suppression of Q_{max} and K_L (Fig 3). In the presence of Ca^{2+}, Q_{max} decreased to 49.0% while K_L decreased up to ~ 68%. The overall inhibition order was Control > Na^+ > Ca^{2+}, consistent with competitive interactions reported for fluoroquinolone adsorption on carbonaceous materials [21,22]. Divalent cations cause much stronger inhibition such as bamboo biochar showed Ca^{2+} disrupting adsorption far more than Na^+ [38].

The strong inhibition by Ca^{2+} is attributable to the substantially larger hydration sphere (hydrated ionic radius ~ 4.12 Å for Ca^{2+} vs. 3.6 Å for Na^+) and its stronger Lewis acid character, which confer two mechanistically distinct inhibitory pathways. First, Ca^{2+} can form stable bidentate chelates with the adjacent 3-carboxyl and 4-keto (oxo) groups on the quinolone core of CFX in solution [39,40] converting free CFX into poorly reactive Ca–CFX complexes and reducing the effective CFX concentration accessible to the adsorbent surface. Second, Ca^{2+} competes directly for the same –COOH and –OH surface sites on the biochar that would otherwise engage in electrostatic attraction and hydrogen bonding with CFX.

Because a divalent cation can occupy two adjacent functional sites simultaneously, its site-blocking efficiency is inherently greater than that of monovalent Na^+ [41]. The stronger affinity of Ca^{2+} for both surface functional groups and the CFX functional group explains its greater inhibitory capacity compared to sodium ions (Na^+). Pre-treatment to remove divalent cations, or the use of biochar with a higher degree of aromatization (and thus less reliance on functional-group-mediated mechanisms) may be necessary to maintain adequate performance in such environments.

3.7. Proposed sorption mechanism

A mechanistic framework is proposed here by integrating the evidence from biochar characterization, sorption kinetics, pH- and temperature-dependent isotherms, thermodynamic analysis, and ionic competition experiments. The carbon-rich composition (87.65 wt%) and the Langmuir surface area of 53.175 $m^2\ g^{-1}$ indicated a moderately developed pore. The kinetic sorption is rapid in first stage of IPD model (k_1 = 2.775 mmol kg^{-1} $min^{-1/2}$), corresponding to external surface adsorption and diffusion through macropores. Thus, the sorption of CFX onto lotus biochar (BC) is governed by surface-driven interactions.

Electrostatic attraction and hydrogen bonding are considered the dominant mechanisms for BC. At the pH 7, the negatively charged BC surface (pH > pH_{pzc} = 6.0) attracts the positively charged piperazinyl nitrogen of zwitterionic $CFX^{\pm}$ ($CFX^{\pm}$, 87.2%) via Coulombic attraction. The Langmuir model yielded the highest Q_{max} (22.96 mmol kg^{-1}) and K_L (65.17 L $mmol^{-1}$). The FTIR shifts observed after CFX sorption at pH 7 specifically the blue shift of the –OH band (3416 → 3438 cm^{-1}), the shift of the aromatic C=C vibration (1612 → 1618 cm^{-1}), and the displacement of the C–O stretching band (1163 → 1178 cm^{-1}), collectively confirm the involvement of hydrogen bonding and π–π stacking. The positive ΔH° (+44.02 kJ mol^{-1}) established the endothermic nature of CFX adsorption, indicating that the energy required to disrupt the hydration shells surrounding both CFX molecules and the biochar surface.

Table 5: Comparison of the Q_{max} of lotus stem biochar with various lignocellulosic and algal biochars reported in the literature.

No.	Biochar	Temp. pyrolysis	Initial pH	Conc. Range (mg L^{-1})	Adsorbent Dose (g L^{-1})	Isotherm model	Q_{max} (mmol kg^{-1}) (unit conversion)	References
1	Rice straw biochar (B5)	500°C	7	2 – 15	1.5	Langmuir	11.2	[32]
2	KOH-modified rice straw biochar (KB5)	500°C	7	2 – 15	1.5	Langmuir	26.4	[32]
3	Corncob	600°C	7	0.1 – 1.2	1.08	Langmuir	1.2	[42]
4	Cassava peel (CP500)	500°C	7	4– 60	2.0	Langmuir	10.5	[4]
5	Cassava peel (CP700)	700°C	7	4 – 60	2.0	Langmuir	11.6	[4]
6	Macadamia nutshell	600°C	7	4 – 60	8	Langmuir	7.4	[8]
7	Brown algae (SW400)	400°C	7	4 – 60	4	Langmuir	11.4	[30]
8	Brown algae (SW600)	600°C	7	4 – 60	4	Langmuir	15.2	[30]
9	Groundnut shell (GNS500)	500°C	7	5 – 30	0.8	Langmuir	6.9	[31]
10	Groundnut shell (GNS900)	900°C	7	5 – 30	0.8	Langmuir	19.3	[31]
11	Wheat straw (WS)	700°C	7	1 – 30	0.1 – 2.2	Langmuir	25.9	[43]
12	Cupuaçu bark AC (H_3PO4, 88%)	600°C	5.0	30 – 330	0.4 – 0.8	Langmuir	18.2	[44]
13	Lotus stem	400°C	3	12 – 80	2.0	Langmuir	~20.6	This study
14	Lotus stem	400°C	7	12 – 80	2.0	Langmuir	~23.0	This study
15	Lotus stem	400°C	10	12 – 80	2.0	Langmuir	~22.9	This study

The large positive ΔS° (+239.66 J mol^{-1} K^{-1}) compensated for this enthalpic cost, rendering the process spontaneous (ΔG° < 0) across all temperatures. The Na^+ reduced Q_{max} by only 9% while divalent Ca^{2+} caused severe suppression of Q_{max} (49%). The stronger inhibition by Ca^{2+} compared to Na^+ confirms that functional-group-mediated interactions (electrostatic attraction and hydrogen bonding) constitute a significant fraction of the total adsorption capacity.

Table 5 compares the Q_{max} of biochar for CFX removal against values reported for other lignocellulosic and marine-derived biochars. At neutral pH, lotus stem biochar exhibited a Q_{max} of ~ 23.0 mmol kg^{-1}, exceeding the capacities reported for conventional agricultural-waste biochars such as corn cob (1.2 mmol kg^{-1}) [42], macadamia nutshell (7.4 mmol kg^{-1}) [8], groundnut shell (6.9 mmol kg^{-1}) [31], cassava peel (10.5 mmol kg^{-1}) [4], and rice straw (11.2 mmol kg^{-1}) [32]. The Q_{max} of lotus stem biochar was also comparable of Cupuaçu bark AC (H_3PO_4, 88%) (18.2 mmol kg^{-1}) or KOH-modified rice straw biochar (26.4 mmol kg^{-1}) [32]. It's noteworthy that the lotus stem biochar was produced without any chemical activation or metal impregnation. Even when benchmarked against brown-algae biochars, which are known for their abundant nitrogen- and oxygen-containing surface functionalities, lotus stem biochar outperformed the 400 °C and 600 °C seaweed biochar (11.4–15.2 mmol kg^{-1}) [30]. The robustness of BC across a wide pH window (Q_{max} of 20.6, 23.0, and 22.9 mmol kg^{-1} at pH 3, 7, and 10, respectively) further differentiates it from most reported biochars. It is important to emphasize that the comparisons presented are for reference only due to significant differences in other experimental conditions, such as temperature, particle size, and ion concentration. Therefore, the purpose of this comparison is only to demonstrate the potential of biochar from lotus stems and not to assert absolute superiority.

4. Conclusions

This study investigated the adsorption of CFX onto unmodified biochar derived from lotus stem pyrolyzed at 400 °C. Adsorption kinetics followed the Two-Stage IPD model with k_1 = 2.775 ± 0.112 mmol kg^{-1} $min^{-1/2}$. The adsorption isotherms could be described by Langmuir

models, with the Q_{max} reaching 22.96 mmol kg^{-1} at pH 7 and 26 °C. Solution pH governed adsorption performance through the interplay of CFX speciation and biochar surface charge. Unmodified biochar can adsorb CFX across all the study pH ranges (3, 7, 10). The highest capacity at pH 7 was attributed to the electrostatic attraction, hydrogen bonding, and π–π EDA. Thermodynamic analysis revealed that CFX sorption onto BC is a spontaneous ($\Delta G° < 0$), endothermic ($\Delta H° = +44.02$ kJ mol^{-1}), and entropy-driven ($\Delta S° = +239.66$ J mol^{-1} K^{-1}) process. However, the presence of divalent cations Ca^{2+} suppressed Q_{max} through competitive sorption with CFX. Overall, unmodified lotus stem biochar stands out as an affordable adsorbent that performs effectively across a broad pH range (3–10) and in tropical conditions. Nonetheless, while Q_{max} is comparable across this range, its underlying interactions differ, and the long-term stability at extreme pH warrants further study. These findings present a sustainable pathway for valorizing lotus agricultural residues into biochar, which can be utilized for the removal of antibiotics from water.

List of Abbreviations:

AICc – Second-order Akaike Information Criterion

adj-R^2 – Adjusted Coefficient of Determination

AMR – Antimicrobial Resistance

BC – Biochar (lotus stem-derived biochar pyrolyzed at 400 °C)

CFX – Ciprofloxacin

EDX – Energy-Dispersive X-ray Spectroscopy

FESEM – Field-Emission Scanning Electron Microscopy

FTIR – Fourier-Transform Infrared Spectroscopy

IPD – Intraparticle Diffusion

PFO – Pseudo-First Order kinetic model

pH_{PZC} – Point of Zero Charge

PSO – Pseudo-Second Order kinetic model

SSA – Specific Surface Area

UV–Vis – Ultraviolet–Visible spectrophotometry

ΔG° – Standard Gibbs free energy change

ΔH° – Standard enthalpy change

ΔS° – Standard entropy change

Author Contributions:

Vo Nguyen Lam Uyen, Vo Duc Hieu, Dang Thanh Minh Khoi: Investigation, Formal analysis, Writing – original draft, Writing – review & editing. Pham Duy Tan: Conceptualization, Writing – original draft, Writing – review & editing. Ly Quoc Nguyen Khang: Conceptualization, Writing – original draft, Writing – review & editing. Nguyen Le The Quang, Nguyen Trong Bang, Phan Trung Hieu: Writing – original draft, Writing – review & editing. Bao-Trong Dang: Methodology, Software, Visualization, Validation, Writing – original draft, Writing – review & editing.

Availability of data and materials:

All data included in this study are available upon request.

Consent for Publication:

Not applicable

Conflicts of Interest:

The author(s) declare no conflicts of interest regarding this manuscript.

Funding:

No external funding was received for this research

Acknowledgments:

We acknowledge Ho Chi Minh City University of Technology (HCMUT), and Vietnam National University Ho Chi Minh City (VNU-HCM) for supporting this study.

AI-declaration:

The authors acknowledge the use of Grammarly® for language editing to improve the clarity and readability of the manuscript during the preparation of this work. After using this tool, the authors reviewed and edited the content as needed and take full responsibility for the content of the manuscript.

References:

[1] Chu L, Wang J, He S, Chen C, Wojnárovits L, Takács E. Treatment of pharmaceutical wastewater by ionizing radiation: Removal of antibiotics, antimicrobial resistance genes and antimicrobial activity. J Hazard Mater 2021;415. https://doi.org/10.1016/j.jhazmat.2021.125724.

[2] Huang A, Yan M, Lin J, Xu L, Gong H, Gong H. A review of processes for removing antibiotics from breeding wastewater. Int J Environ Res Public Health 2021;18. https://doi.org/10.3390/ijerph18094909.

[3] Zheng D, Wu M, Zheng E, Wang Y, Feng C, Zou J, et al. Parallel adsorption of low concentrated ciprofloxacin by a CoFe-LDH modified sludge biochar. J Environ Chem Eng 2022;10. https://doi.org/10.1016/j.jece.2022.108381.

[4] Dang BT, Tran CHB, Pham TLN, Duong NHN, Do TAS, Son Nguyen T, et al. Hierarchical factors governing the removal of ionizable pharmaceuticals by cassava peel–derived biochar: Bayesian modeling and DFT approaches. Results in Engineering 2026;30. https://doi.org/10.1016/j.rineng.2026.110528.

[5] Ghanadi M, Milke M, Larcher S, Mackey HR, Bello-Mendoza R. Critical review of antimicrobials, antimicrobial resistance, and their associated genes in decentralized wastewater treatment systems. J Environ Chem Eng 2026;14. https://doi.org/10.1016/j.jece.2026.121039.

[6] The Lancet. Antimicrobial resistance: an agenda for all. The Lancet 2024;403:2349. https://doi.org/10.1016/S0140-6736(24)01076-6.

[7] Sambaza SS, Naicker N. Contribution of wastewater to antimicrobial resistance: A review article. J Glob Antimicrob Resist 2023;34:23–9. https://doi.org/10.1016/j.jgar.2023.05.010.

[8] Na PT Le, Tuyen NDK, Dang BT. Sorption of four antibiotics onto pristine biochar derived from macadamia nutshell. Bioresour Technol 2024;394:130281. https://doi.org/10.1016/j.biortech.2023.130281.

[9] Yang Z, Xing R, Zhou W, Zhu L. Adsorption characteristics of ciprofloxacin onto g-MoS2 coated biochar nanocomposites. Front Environ Sci Eng 2020;14. https://doi.org/10.1007/s11783-019-1218-0.

[10] Zhao B, O'Connor D, Zhang J, Peng T, Shen Z, Tsang DCW, et al. Effect of pyrolysis temperature, heating rate, and residence time on rapeseed stem derived biochar. J Clean Prod 2018;174:977–87. https://doi.org/10.1016/j.jclepro.2017.11.013.

[11] Xue Y, Guo Y, Zhang X, Kamali M, M. Aminabhavi T, Appels L, et al. Efficient adsorptive removal of ciprofloxacin and carbamazepine using modified pinewood biochar – A kinetic, mechanistic study. Chemical Engineering Journal 2022;450. https://doi.org/10.1016/j.cej.2022.137896.

[12] Pan Y, Han G, Mao Z, Zhang Y, Duan H, Huang J, et al. Structural characteristics and physical properties of lotus fibers obtained from Nelumbo nucifera petioles. Carbohydr Polym 2011;85:188–95. https://doi.org/10.1016/j.carbpol.2011.02.013.

[13] Feng Z, Chen N, Feng C, Gao Y. Mechanisms of Cr(VI) removal by FeCl3-modified lotus stem-based biochar (FeCl3@LS-BC) using mass-balance and functional group expressions. Colloids Surf A Physicochem Eng Asp 2018;551:17–24. https://doi.org/10.1016/j.colsurfa.2018.04.054.

[14] Hou Y, Liang Y, Hu H, Tao Y, Zhou J, Cai J. Facile preparation of multi-porous biochar from lotus biomass for methyl orange removal: Kinetics, isotherms, and regeneration studies. Bioresour Technol 2021;329. https://doi.org/10.1016/j.biortech.2021.124877.

[15] Li X, Wang Y, Chen C, Tian C, Yu X, Liu J, et al. Sustainable biochar derived from waste lotus seedpod for efficient adsorption of residual carbamate pesticides. Heliyon 2025;11. https://doi.org/10.1016/j.heliyon.2025.e42741.

[16] Wang Y, Lin R, Zhang L, Han X, Li J, Huang C, et al. ZrO2-MoO3/modified lotus stem biochar catalysts for catalytic aquathermolysis of heavy oil at low-temperature. Fuel 2024;357:129597. https://doi.org/https://doi.org/10.1016/j.fuel.2023.129597.

[17] Bui TX, Choi H. Adsorptive removal of selected pharmaceuticals by mesoporous silica SBA-15. J Hazard Mater 2009;168:602–8. https://doi.org/10.1016/j.jhazmat.2009.02.072.

[18] Afzal MZ, Sun X-F, Liu J, Song C, Wang S-G, Javed A. Enhancement of ciprofloxacin sorption on chitosan/biochar hydrogel beads. Science of The Total Environment 2018;639:560–9. https://doi.org/https://doi.org/10.1016/j.scitotenv.2018.05.129.

[19] Zhao J, Liang G, Zhang X, Cai X, Li R, Xie X, et al. Coating magnetic biochar with humic acid for high efficient removal of fluoroquinolone antibiotics in water. Science

of The Total Environment 2019;688:1205–15. https://doi.org/https://doi.org/10.1016/j.scitotenv.2019.06.287.

[20] Sumita, Wang Y, Yu J, Li C. Iron-modified biochar for enhanced removal of ciprofloxacin and amoxicillin in wastewater. Environ Chem Lett 2025;23:27–32. https://doi.org/10.1007/s10311-024-01792-6.

[21] Guan X, Guo J, Zhang H, Tao S, Mailhot G, Wu F, et al. Effect of Co-Existing Cations and Anions on the Adsorption of Antibiotics on Iron-Containing Minerals. Molecules 2022;27. https://doi.org/10.3390/molecules27228037.

[22] Wang J, Li X, Lan Y, Wang H, Ma X, Wang H, et al. Study on the adsorption mechanism of ciprofloxacin in wastewater by modified fly ash under the coexistence of copper. J Environ Chem Eng 2024;12. https://doi.org/10.1016/j.jece.2024.114336.

[23] Chen J, Liu Y, Liu J, Duan Q, Wang Z, Song J, et al. Effects of carbonization on the structure and sorption properties of coffee grounds for Pb(II) and Ni(II) in various metal systems. Desalination Water Treat 2024;320. https://doi.org/10.1016/j.dwt.2024.100623.

[24] Kumar NV, Sawargaonkar GL, Rani CS, Singh A, Prakash TR, Triveni S, et al. Comparative Analysis of Pigeonpea Stalk Biochar Characteristics and Energy Use under Different Biochar Production Methods. Sustainability (Switzerland) 2023;15. https://doi.org/10.3390/su151914394.

[25] Gutierrez-Martinez J, Martinez-Vargas DR, Vences-Alvarez E, Arjona-Jaime P, López-Cázares MI, Rios-Saldaña LE, et al. Point of zero charge, isoelectric point, and potential of zero charge on activated carbons: A comprehensive interpretation about their interrelation. Curr Opin Solid State Mater Sci 2026;40. https://doi.org/10.1016/j.cossms.2025.101247.

[26] Zhang L, Ren Y, Xue Y, Cui Z, Wei Q, Han C, et al. Preparation of biochar by mango peel and its adsorption characteristics of Cd(ii) in solution. RSC Adv 2020;10:35878–88. https://doi.org/10.1039/d0ra06586b.

[27] Czyrski A. The spectrophotometric determination of lipophilicity and dissociation constants of ciprofloxacin and levofloxacin. Spectrochim Acta A Mol Biomol Spectrosc 2022;265. https://doi.org/10.1016/j.saa.2021.120343.

[28] Thao NTP, Le Na PT, Huynh KPH, Dang BT. Comparison of porous and non-porous biochar for trimethoprim removal: Quantifying uncertainty in sorption and thermodynamic parameters over different pH and temperature. Case Studies in Chemical and Environmental Engineering 2025;12:101264. https://doi.org/10.1016/j.cscee.2025.101264.

[29] Le Na PT, Quang NLT, Thao NTP, Chi HTK, Dang BT. Harnessing corncob-derived materials for the elimination of sulfamethoxazole from water. Bioresour Technol Rep 2025;29. https://doi.org/10.1016/j.biteb.2025.102050.

[30] Nguyen TPT, Nguyen LTQ, Pham TLN, Bao-Trong D. Bayesian and unsupervised learning insights into pH- and temperature-driven sorption of fluoroquinolones and sulfonamides on marine algal biochar. Chemosphere 2025;392:144753. https://doi.org/10.1016/j.chemosphere.2025.144753.

[31] Alawa B, Singh S, Chakma S, Kishor R, Vinu R, Stålsby Lundborg C, et al. Mechanistic investigations on sorption of ciprofloxacin from water using groundnut shell derived biochar. Results in Engineering 2026;29. https://doi.org/10.1016/j.rineng.2025.108812.

[32] Wang H, Wang H, Shahab S, Cheng H, Atroshko M, Wang X, et al. Enhanced adsorption of ciprofloxacin by biochar with acid and alkali modification: Performance comparison and mechanism analysis. Results Chem 2025;17. https://doi.org/10.1016/j.rechem.2025.102603.

[33] Rauch R, Lukács É, Molnár M. Adsorptive removal of 2,4-dichlorophenol from aqueous solution using micronized oil shale. Adsorption 2025;31:1–11. https://doi.org/10.1007/s10450-024-00570-8.

[34] Lin H, Qiu S, Wu Z, Ye X, Liu M. Fabrication of lignin-based biochar containing multi-metal ferrite and efficient removal for oxytetracycline hydrochloride. J Clean Prod 2022;331:129885. https://doi.org/10.1016/j.jclepro.2021.129885.

[35] Ferreiro EA, de Bussetti SG. Thermodynamic parameters of adsorption of 1,10-phenanthroline and 2,2′-bipyridyl on hematite, kaolinite and montmorillonites. Colloids Surf A Physicochem Eng Asp 2007;301:117–28. https://doi.org/10.1016/j.colsurfa.2006.12.032.

[36] Liu X, Lu S, Liu Y, Meng W, Zheng B. Adsorption of sulfamethoxazole (SMZ) and ciprofloxacin (CIP) by humic acid (HA): Characteristics and mechanism. RSC Adv 2017;7:50449–58. https://doi.org/10.1039/c7ra06231a.

[37] Falyouna O, Maamoun I, Idham MF, Eljamal O. Effect of water matrix on ligand-assisted adsorption of ciprofloxacin from aqueous solutions by zerovalent iron nanoparticles. International Exchange and Innovation Conference on Engineering and Sciences, Kyushu University; 2022, p. 62–7. https://doi.org/10.5109/5909063.

[38] Peng X, Hu F, Lam FLY, Wang Y, Liu Z, Dai H. Adsorption behavior and mechanisms of ciprofloxacin from aqueous solution by ordered mesoporous carbon and bamboo-based carbon. J Colloid Interface Sci 2015;460:349–60. https://doi.org/10.1016/j.jcis.2015.08.050.

[39] Pitman SK, Hoang UTP, Wi CH, Alsheikh M, Hiner DA, Percival KM. Revisiting oral fluoroquinolone and multivalent cation drug-drug interactions: Are they still relevant? Antibiotics 2019;8. https://doi.org/10.3390/antibiotics8030108.

[40] Walden DM, Khotimchenko M, Hou H, Chakravarty K, Varshney J. Effects of magnesium, calcium, and aluminum chelation on fluoroquinolone absorption rate and bioavailability: A computational study. Pharmaceutics 2021;13. https://doi.org/10.3390/pharmaceutics13050594.

[41] Zeng ZW, Tan XF, Liu YG, Tian SR, Zeng GM, Jiang LH, et al. Comprehensive adsorption studies of doxycycline and ciprofloxacin antibiotics by biochars prepared at different temperatures. Front Chem 2018;6. https://doi.org/10.3389/fchem.2018.00080.

[42] Dang BT, Gotore O, Ramaraj R, Unpaprom Y, Whangchai N, Bui XT, et al. Sustainability and application of corncob-derived biochar for removal of fluoroquinolones. Biomass Convers Biorefin 2022;12:913–23. https://doi.org/10.1007/s13399-020-01222-x.

[43] Alawa B, Singh S, Chakma S, Kishor R, Stålsby Lundborg C, Diwan V. Development of novel biochar adsorbent using agricultural waste biomass for enhanced removal of ciprofloxacin from water: Insights into the isotherm, kinetics, and thermodynamic analysis. Chemosphere 2025;375:144252.

[44] do Nascimento RA, Novaes N dos R de O, Morilla DP, da Luz PTS, Costa CML, Faria LJG de. Removal of Ciprofloxacin and Norfloxacin from Aqueous Solution with Activated Carbon from Cupuaçu (Theobroma grandiflorum) Bark. Molecules 2024;29.